

Journal of Biomedical Optics

SPIEDigitalLibrary.org/jbo

Multispectral optoacoustic tomography at 64, 128, and 256 channels

Alexander Dima
Neal C. Burton
Vasilis Ntziachristos

Multispectral optoacoustic tomography at 64, 128, and 256 channels

Alexander Dima,^{a,b} Neal C. Burton,^c and Vasilis Ntziachristos^{a,b,*}

^aInstitute for Biological and Medical Imaging, Helmholtz Zentrum München, Ingolstädter Landstrasse 1, Neuherberg 85764, Germany

^bTechnische Universität München, Department of Medicine and Department of Electrical Engineering and Information Technology, Chair for Biological Imaging, Arcisstrasse 21, Munich 80333, Germany

^cThera Medical GmbH, Zielstattstrasse 13, Munich 81379, Germany

Abstract. Optoacoustic (photoacoustic) imaging has already showcased the capacity to offer high-resolution small animal visualization *in vivo* in a variety of cancer, cardiovascular, or neuroimaging applications. In particular, multispectral optoacoustic tomography (MSOT) has shown imaging along the spectral and the time dimensions, enabling sensing of multiple molecules over time and, more recently, in real time. Furthermore, cross-sectional imaging of at least 20 mm diameter has been showcased *in vivo* in animals and humans using 64-element curved transducers placed along a single curved line. Herein, we investigated the imaging improvements gained by utilizing a larger number of detectors and inquired whether more detectors will result in measurable image quality improvements. For this reason, we implemented MSOT using 64-, 128-, and 256-element transducers and imaged the same phantoms and animals under similar conditions. Further, corroborated by numerical simulation analysis, our findings quantify the improvements in resolution and overall image quality for the increasing number of detectors used pointing to significant improvements in image quality for the 256 detector array, over 64 or 128 detectors. © 2014 Society of Photo-Optical Instrumentation Engineers (SPIE) [DOI: [10.1117/1.JBO.19.3.036021](https://doi.org/10.1117/1.JBO.19.3.036021)]

Keywords: optoacoustics; tomography; imaging systems.

Paper 130728RR received Oct. 9, 2013; revised manuscript received Jan. 27, 2014; accepted for publication Feb. 25, 2014; published online Mar. 27, 2014.

1 Introduction

Noninvasive imaging has become an important modality in small-animal research by enabling longitudinal insights *in vivo* and on the same animal. Radiological imaging systems adapted from clinical use are routinely employed to visualize anatomical and molecular features, e.g., computed tomography (CT) / magnetic resonance imaging (MRI) and single-photon emission computed tomography (SPECT) / positron emission tomography (PET).^{1,2} Optical imaging has also emerged as a valuable investigative method. In addition to the central role that optical microscopy plays in biological interrogation, bioluminescence and fluorescence epi-illumination planar imaging and fluorescence molecular tomography³ have been disseminated in the biological and drug discovery laboratory. A major limitation, however, of optical imaging has been the limited resolution achieved for penetration depths >0.5 to 1 mm due to the strong photon scattering by tissues. For this reason, optoacoustic (photoacoustic) imaging methods are increasingly considered as they can improve the resolution and optical imaging accuracy achieved over conventional optical methods, when imaging through several millimeters to centimeters of tissue.

Optoacoustic imaging operates on the local thermoelastic expansion of tissue, following absorption of transient light intensity incident on the tissue.⁴ The thermoelastic expansion generated by different tissue photoabsorbing molecules yields broad-band ultrasonic waves, which can be sensed by ultrasound detectors. Image formation then requires the placement of

detectors at multiple locations around the tissue of investigation and the subsequent processing of the data collected and their mathematical inversion (tomography) in order to produce images of the magnitude and location of the various photoabsorbing molecules present in the tissue.⁵ By illuminating tissue at multiple wavelengths and using spectral detection (unmixing) techniques, multispectral optoacoustic tomography can then resolve multiple intrinsic tissue constituents or extrinsically administered agents and nanoparticles.^{6,7}

Several optoacoustic implementations have been shown to achieve small animal imaging in two (2-D) and three (3-D) dimensions. Systems have been implemented using single detectors that are scanned in one or more dimensions,^{8–10} one-dimensional linear, curved, or circular detector arrays,^{11–14} or 2-D detector arrangements^{15–17} that place detectors on planar or curved surfaces. A recently developed 3-D real-time optoacoustic system using a 2-D curved detector with 256 elements¹⁶ traded in-plane resolution in favor of parallel volumetric scanning. In order to achieve high resolution and 3-D imaging, other 3-D systems operate by scanning the detectors employed to achieve higher spatial sampling of optoacoustic signals. A major challenge of 3-D imaging in this case is the long acquisition times typically required to obtain high-quality datasets.

Two-dimensional imaging implementations, therefore, have a significant advantage over 3-D imaging systems. By using one-dimensional arrays they can concentrate the number of detectors available for achieving high in-plane resolution. Out-of-plane signals can then be rejected by utilizing acoustically focused detectors.

*Address all correspondence to: Vasilis Ntziachristos, E-mail: v.ntziachristos@tum.de

In this mode, 2-D systems have been shown to achieve video-rate imaging of tissue cross-sections at a single wavelength¹⁸ or, more recently, at multiple wavelengths.¹⁹ Video-rate imaging is important for ensuring fast tissue interrogation, monitoring dynamic events, and minimizing motion artifacts that are present in scanning systems. It would be possible to develop systems based on 2-D arrays using a large number of detectors to allow for high-quality video-rate 3-D imaging. However, such implementations are currently largely impractical as they would require thousands of detectors in order to achieve the same in-plane resolution as 2-D imaging systems. Besides challenges associated with complexity and cost, a further challenge of 3-D systems is that they require illumination of entire volumes, which reduces the signal-to-noise ratio available to each of the 2-D images produced from the volume. Instead, one-dimensional array systems operate by concentrating the light energy available around the circumference of the tissue slice imaged, so that sources of lower power and, therefore, cost can be utilized.

We previously introduced a one-dimensional curved array system optimized for high throughput, small-animal full-body imaging¹⁸ and highlighted several *in vivo* applications in small animal imaging using this technology.^{6,20–22} A variant of the system was introduced as a handheld device imaging the carotids and various other vessels and human tissue parts *in vivo*,²³ also, more recently, demonstrating multispectral imaging at video rates using a high-rate fast wavelength tuning laser.¹⁹ Despite the high-resolution imaging performance achieved, most imaging studies were performed using a 64-element one-dimensional curved array. Here we wanted to gain insights into the improvement achieved with higher-density detectors and whether doubling and quadrupling the number of elements would lead to observable and desirable imaging improvement. Therefore, we implemented multispectral optoacoustic tomography (MSOT) using detector arrays with 64, 128, and 256 elements and compared their relative performance. Experimental comparisons included imaging the same phantoms and interrogating the resolution, effective region of interest, image quality, and sensitivity achieved with the different detectors. These findings were also corroborated by numerical simulations. Finally, to showcase achievable imaging performance, we present a comparative study performed *in vivo* on the same healthy mouse measured by all three systems within a short amount of time. We conclude that significant improvements in image quality, region of interest, and sensitivity are observed with an increasing number of detectors to justify the investment of utilizing denser arrays for MSOT.

2 Materials and Methods

2.1 Acoustic Detection

All three arrays employed in this study were custom-made cylindrically focused curved arrays (Imasonic S.A., France) with varying geometrical properties, yet manufactured from the same piezocomposite material to cover the frequency band up to 7.5 MHz with peak sensitivity at 5 MHz. To facilitate a concise description for the remainder of this text, we introduce a nomenclature based on the number of elements per array: MSOT64 (64 elements), MSOT128 (128 elements), and MSOT256 (256 elements). Figure 1 illustrates apertures and overall arrangements of the three systems (left column MSOT64, right column MSOT128/256) and defines the coordinate system, which we will refer to in the following. The

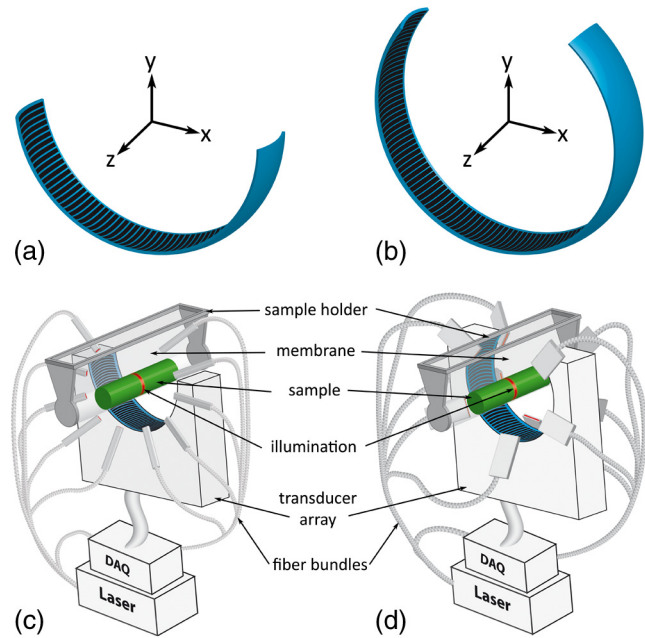


Fig. 1 The first row shows the transducer geometries for (a) MSOT64 and (b) MSOT128/MSOT256. The second row illustrates the two system setups, including laser, data acquisition (DAQ), and sample holder with transparent membrane. (c) MSOT64 achieves even in-plane ($z = 0$) illumination by using a ten arm fiber bundle arranged from one side at an angle of 33 deg relative to the circumference of the sample. (d) MSOT128/256 enables similar illumination by arranging a second ten arm fiber bundle symmetrically from both sides at an angle of 24 deg. Both fiber bundles cover an angle of 270 deg in the xy -plane.

geometric characteristics of all three arrays and their respective single elements are summarized in Table 1.

The MSOT64 geometry is depicted in Fig. 1(a). We define the origin of the coordinate system to coincide with the center of the hypothetical sphere described by the array such that the xy -plane at $z = 0$ represents the imaging plane offering a cross-sectional view of the object. Translation along the z axis, thereby, enables full-body imaging. At $z = 0$ the extended length of the curvature in elevation constitutes cylindrical focusing along the z axis, while the comparably small pitch allows a sufficient field of view (FOV) for tomographic imaging in the xy -plane. As the elements of all three arrays in this study are composed of the same piezocomposite material, but with varying geometrical sizes, we chose as the norm a single element of the MSOT64 and gave it the area size and sensitivity of 100%. Both measures were determined by the manufacturer using standardized protocols and are, thus, comparable between arrays.

MSOT128, depicted in Fig. 1(b), enables a more complete tomographic view, which is expected to significantly improve image quality. A smaller pitch increases the FOV of a single element and, thereby, should improve transversal resolution, i.e., perpendicular to the radius. Consequently, single element area size is only 72% of the MSOT64 norm and the sensitivity 55%. Nonetheless, due to twice the number of elements compared to MSOT64, the resulting full array sensitivity within areas of overlapping FOV should be 110%.

MSOT256 shares most of the geometrical characteristics with MSOT128 and is also characterized by Fig. 1(b). However, the system employs twice the number of elements, whose elevation focus is closer ($R_{sc} = 37$ mm) compared to

Table 1 Geometric specifications (SE = single element).

	Azimuth span Φ (deg)	Elevation span ϑ (deg)	Array radius R_A	SE radius R_{se}	SE pitch p (mm)	SE length L (mm)
MSOT64	172	21.6	40	40	1.880	15.08
MSOT128	270	20.2	40	40	1.470	14.10
MSOT256	270	21.6	40	37	0.735	13.95

the in-plane array focus ($R_A = 40$ mm). This geometry is expected to achieve the largest FOV and the best transversal resolution. Even though the area size of a single element is merely 36% of the MSOT64 norm and corresponding sensitivity 29%, total sensitivity of the MSOT256 is expected to be 114% within overlapping FOV.

Using an ultrasound field simulation program [Field II (Refs. 24 and 25)] and the geometrical characteristics of a single element, we have numerically simulated the expected sensitivity field up to 7.5 MHz in the imaging plane ($z = 0$) for the single elements of each array—sensitivity being defined here as the maximum expected amplitude from a given position $(x, y, 0)$. By appropriately rotating and summing single element sensitivity fields we can obtain compound sensitivity fields for the three arrays employed (Fig. 2). The short solid lines marked by arrows and an element number on the images indicate the first and last element of the transducer. Black ellipses designate the region of full-width half-maximum (FWHM), i.e., where the amplitude drops to at most 50% of the peak value. For MSOT64, depicted

in Fig. 2(a), the expected field is characterized by a diameter at FWHM of 15.5 mm and a small displacement from the center of the array, due to the limited coverage of 172 deg. For MSOT128, shown in Fig. 2(b), calculations show a horizontal extent of 21 mm and a vertical extent of 17.1 mm, due to the asymmetric distribution of detectors. The reduced pitch and toroidal focusing of MSOT256 elements result in an FWHM diameter of 32.6 mm, shown in Fig. 2(c).

A second parameter relating to image quality is the angular coverage of the imaging plane. It has been shown²⁶ that boundaries, whose normals do not pass through at least one detection element, are invisible and after reconstruction lead to blurring or reconstruction artifacts.²⁷ For better understanding, Figs. 2(d) and 2(e) characterize visibility for MSOT64 and MSOT128/256, respectively. The detection or visibility region is, thereby, highlighted in gray and marks the region in which reconstruction of all features and boundaries is stable. The complementary white region with the dashed circle, on the other hand, allows only some boundaries to be reconstructed stably.

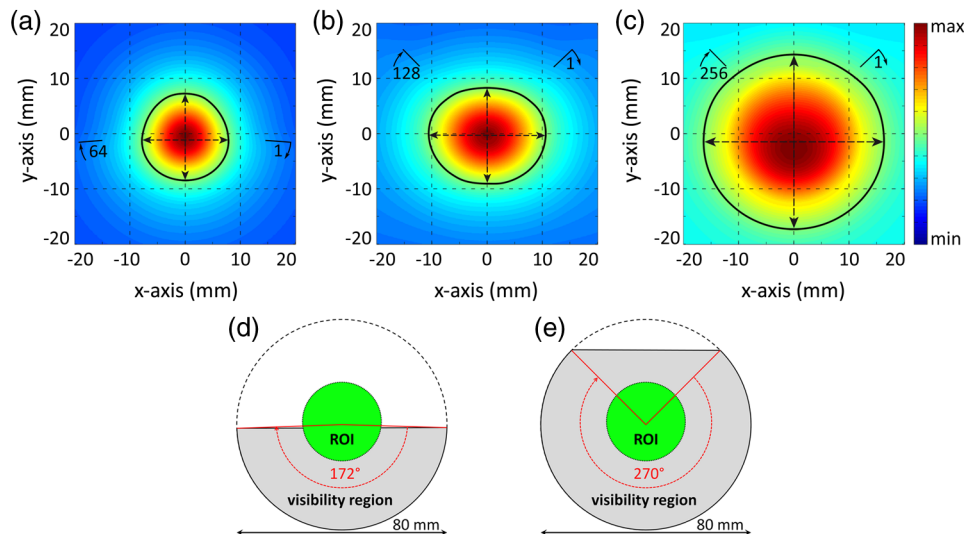


Fig. 2 Theoretical calculation of the two-dimensional sensitivity field of detection (0.5 to 7.5 MHz) within the imaging plane of the detector. Black ellipses mark the full-width half-maximum (FWHM) range. The first and last element of each array is noted on the images by a short solid line marked with an arrow and element number. (a) 64 element array covering 172 deg; diameter at FWHM: 15.5 mm. (b) 128 element array covering 270 deg; vertical diameter at FWHM: 17.1 mm; horizontal diameter at FWHM: 21.0 mm. (c) 256 element array covering 270 deg; diameter at FWHM: 32.6 mm. (d) Visibility region (gray) for MSOT64 and (e) MSOT128/256 that allows stable reconstruction of feature boundaries (ROI, region of interest).

In MSOT64, less than half of a 30-mm-diameter region of interest (ROI) lies within the visibility region, while for MSOT128/256 the ROI is fully covered.

2.2 Experimental Arrangement

The experimental arrangement utilized was comparable to a system previously described.^{18,28} Measurements employed a wavelength tunable pulsed laser (Phocus™, Opotek Inc., USA) with a pulse duration of <10 ns, repetition rate of 10 Hz, and peak pulse energy of 90 mJ at 750 nm. The laser beam was coupled into a ten arm fiber bundle. The MSOT64 system employed a bundle with rectangular outputs of size $3.2 \times 0.72 \text{ mm}^2$ at the distal end. The arms were arranged over an arc of 270 deg next to the detection array, as shown in Fig. 1(c), and established ring illumination at the imaging plane. The systems housing the MSOT128 and MSOT256 employed a slightly different illumination arrangement, depicted in Fig. 1(d). Ring illumination was implemented by five rectangular outputs of $12.4 \times 0.2 \text{ mm}^2$ size covering 270 deg in azimuth on both sides of the arrays. In all setups, the maximum light fluence at the surface of a cylinder of diameter 20 mm, as depicted in Fig. 1, did not exceed 17 mJ/cm^2 at 750 nm. Each array was connected to a custom-made data acquisition (DAQ) system that digitized up to 512 channels in parallel at 10 Hz repetition rate and 40 MSamples/s. All DAQs low-pass filtered the input signals at 15 MHz to avoid aliasing and subsequently amplified them by the same gain. The three detection systems (DAQ + array) had comparable electrical impulse responses, an instance of which was used to deconvolve all signals prior to reconstruction.

Image reconstruction was performed using a model-based algorithm.²⁹ The algorithm computes a model-matrix that links measured pressure values with a discrete grid of positions (image pixels) in the imaging plane by numerically evaluating the forward solution of the optoacoustic wave equation. Model inversion was achieved using a regularized iterative least-squares algorithm. All imaging results presented in this study were attained using the same set of parameters, i.e., 450×450 pixels over $30 \times 30 \text{ mm}^2$. Due to the large model-matrix and iterative inversion, reconstruction time per image necessitated offline reconstruction after the data acquisition.

2.3 Numerical Simulation

To facilitate objective observations between the three detectors, we employed numerical simulations. The simulations assumed a rectangular region of $30 \times 30 \text{ mm}^2$ centered at the origin in

the xy -plane ($z = 0$) and placed 900 microspheres equally spaced by 1 mm in x - and y -direction. Figure 3(a) shows the numerical setup, which also represents the reconstruction target. To obtain acoustic data for the three arrays, we first employed an ultrasound field simulation program [Field II (Refs. 24 and 25)] to compute the acoustic field received by each detection element following a Dirac-like excitation at the 900 microsphere positions. Then we convolved these geometric impulse responses, sampled at 40 MSamples/s, with the analytical optoacoustic signal emitted by a spherical absorber³⁰ and obtained acoustic data frames of size 2030×64 , 2030×128 , and 2030×256 . Microsphere size was chosen to span six acoustic samples at 40 MSamples/s, i.e., 125 ns or $187.5 \mu\text{m}$ at 1500 m/s speed of sound.

2.4 Phantoms

Known phantoms were also employed to provide for control measurements that could compare the performance of the three detectors employed. Validation of numerical results was achieved using black polyethylene (PE) microspheres of diameters ranging from 180 to $212 \mu\text{m}$ (Cospheric LLC, USA). Due to practical difficulties replicating the regular sampling grid used in the numerical simulation, we decided to implement an irregularly sampled disk of 30 mm diameter. For this, we prepared a cylindrical tissue mimicking agar (2% w/v) phantom of 50 mm height and 30 mm diameter including a fatty emulsion imparting a reduced scattering coefficient of $\mu'_s = 10 \text{ cm}^{-1}$. The phantom also included a cylindrical cavity at the bottom of 25 mm length and 8 mm diameter. We then dispersed microspheres on top of the phantom aiming to achieve an as even distribution as possible. This way the microspheres described an absorbing disk, which was illuminated from one side through $\sim 25 \text{ mm}$ of scattering agar using a cylindrical fiber bundle inserted through the bottom cavity of the phantom. Fluence variations within the disk were captured by a CCD camera at 680 nm and these measurements were later employed for correction of the reconstructed image. Figure 3(b) shows the acquired photograph from the back-illuminated microsphere layer.

2.5 Mouse Imaging In Vivo

To extend numerical and phantom findings to tissue observations, we imaged an eight-week-old female CD-1® nude mouse *in vivo* (Charles River Laboratories, Germany). Animal handling was conducted in compliance with protocols approved by the Bavarian Animal Research Authority. The animal was

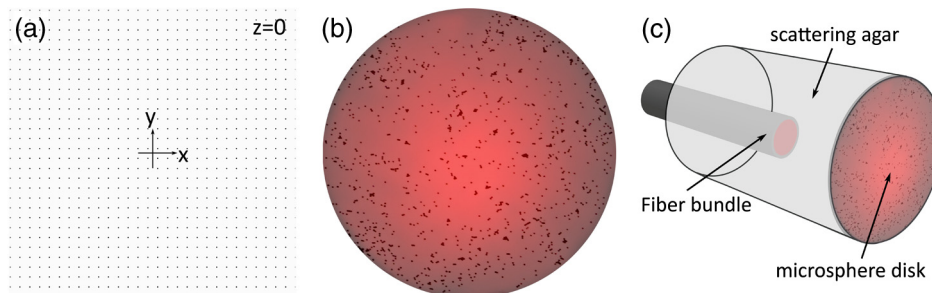


Fig. 3 (a) Numerical setup covering a rectangular region of $30 \times 30 \text{ mm}^2$ —900 microspheres of $187.5 \mu\text{m}$ diameter equally spaced in 1 mm steps. (b) Top view photograph of the microsphere-containing phantom showing the sphere distribution and the fluence distribution. The disk diameter was 30 mm; the polyethylene spheres attained diameters of 180 to $212 \mu\text{m}$. (c) Schematic of the experimental phantom assembly.

anesthetized using 1.8% Isoflurane (Forene®, Abbott AG, Switzerland) vaporized in 100% oxygen at 0.8 L/min and subsequently placed within an animal holder, as described in Ref. 28, in a supine position relative to the arrays. The holder, designed to fit into all three systems, ensured identical positioning of the animal in relation to the detector for the three experimental arrangements. The imaging protocol involved a single-wavelength full-body scan at 850 nm with a step size of 0.5 mm. At each step we recorded 50 frames to capture periodically occurring motion induced by heart beat or breathing. This imaging sequence was repeated for all three systems.

3 Results

3.1 Numerical Simulation

Results obtained from numerical simulation are shown in Fig. 4. Figure 4(a) corresponds to the reconstruction obtained from MSOT64, Fig. 4(b) from MSOT128, and Fig. 4(c) from MSOT256. All images were normalized to 1 and negative values were set to zero as they have no physical meaning. Two rectangular regions ($4 \times 4 \text{ mm}^2$) from the center and the periphery of each array are shown magnified at the bottom of each of the images they were taken from. The images demonstrate two major differences. First, a broader region of the object is visualized for an increasing number of elements employed, as predicted by the sensitivity fields of Fig. 2. The second difference regards transversal resolution, i.e., the resolution perpendicular

to radial lines originating in the middle of the image. Close to the array center, all systems reconstruct the simulated microspheres with a similar performance and accuracy in obtaining their actual dimensions as shown at the bottom right magnification insets in Figs. 4(a) to 4(c). However, the further from the image center a microsphere is positioned, the more its reconstruction is transversally elongated. The strength of this effect is directly related to the pitch of the detector elements in each array, i.e., MSOT64 elements have the largest pitch and cause the strongest distortions; MSOT256 elements have the smallest pitch and the least distortions. The bottom-left magnification insets in Figs. 4(a) to 4(c) illustrate this effect.

A quantitative assessment of both improvements seen as a function of detector elements employed is given in Figs. 4(d) and 4(e), which show a profile (cross-section) of the six magnified images from top-left to bottom-right. Close to the image center, Fig. 4(e), all geometries correctly resolve a microsphere diameter of $190 \mu\text{m}$ at FWHM with comparable sensitivity (amplitude). The noise appearing between the four distinct peaks is a consequence of the high resolution and large imaging region chosen ($30 \times 30 \text{ mm}^2$), which required a degree of regularization inversely proportional to the number of detectors, i.e., stronger for MSOT64 than for MSOT256. On the other hand, transversal resolution at 10 mm distance from the array center, shown in Fig. 4(d), drops for all systems. MSOT64 resolves elongated microspheres of length $\sim 730 \mu\text{m}$; MSOT128 achieves $450 \mu\text{m}$ and MSOT256 $270 \mu\text{m}$ for an actual microsphere size of $187.5 \mu\text{m}$. On the radial axis, all systems resolve

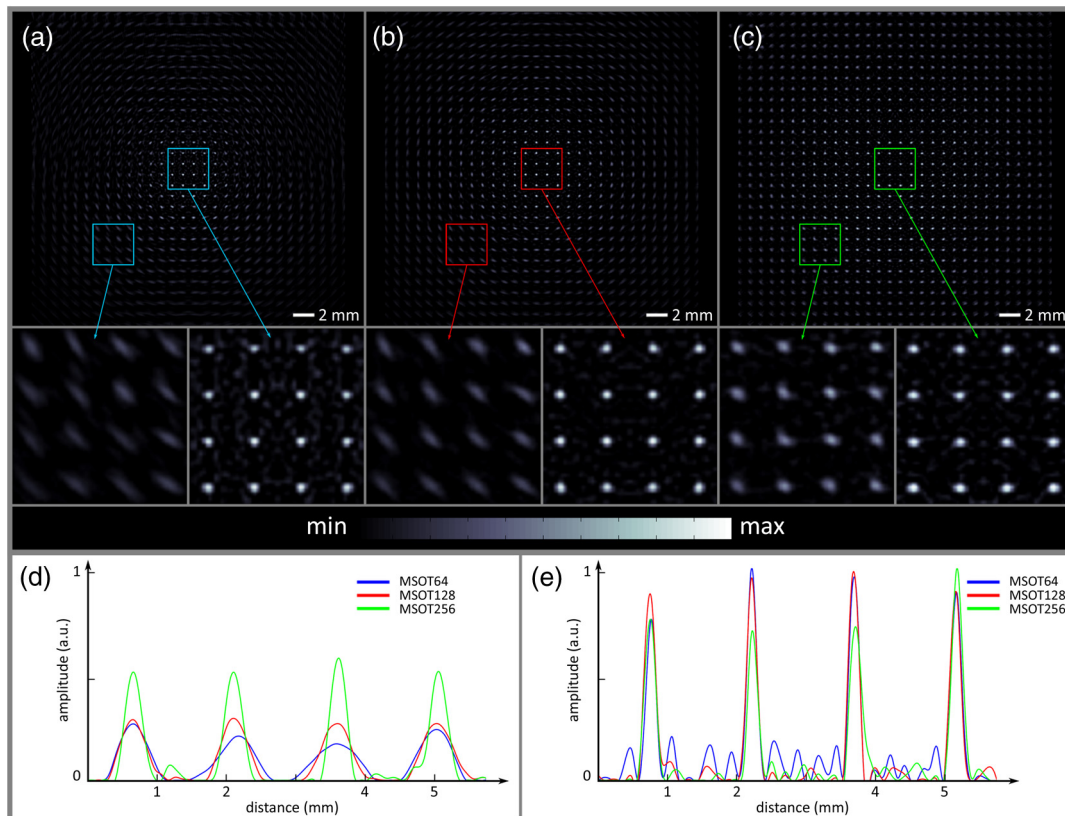


Fig. 4 Top row shows simulated reconstruction results from (a) MSOT64, (b) MSOT128, and (c) MSOT256. For each image, negative values were removed and the remainder normalized to 1. Details at the periphery and the center, framed ($4 \times 4 \text{ mm}^2$) and color-coded by array, were magnified for display at the bottom left and right, respectively. Graphs below depict diagonal cross-sections (top-left to bottom-right) of the magnified detail images for (d) the periphery and (e) the center.

microsphere width as $\sim 250 \mu\text{m}$. Figures 4(d) and 4(e) also illustrate the drop in amplitude when moving further from the array center. While all systems exhibit reduced sensitivity with increasing distance from the center, the drop is sharpest for MSOT64 and marginally better for MSOT128. By contrast, MSOT256 achieves twice the sensitivity of MSOT64.

3.2 Phantom Measurements

Experimental results from the PE microsphere phantom are shown in Fig. 5, which follows a figure arrangement similar to Fig. 4. Due to irregular sampling, we selected three central (4 to 6) and three peripheral (1 to 3) microspheres, which were captured sufficiently well by all geometries, and plotted their transversal profiles in Figs. 5(d) and 5(e). We note that variations in amplitude and shape within close spatial proximity, e.g., within the magnification insets, are due to experimental imperfections such as microsphere clustering, see Fig. 3(b), alignment between phantom and array center or elevational displacement of individual microspheres (on the order of hundreds of micrometer along z axis). Nonetheless, selected microspheres confirmed the observations derived from numerical simulation. In particular, microspheres 4 to 6 from the array center show similar shapes, amplitudes, and resolutions for all systems. Figure 5(e) shows profiles obtained along the diameter of the microspheres revealing an FWHM of $\sim 200 \mu\text{m}$ for all detectors employed. Conversely, selected microspheres (1 to 3) from

the periphery were resolved with different diameters as a function of the number of detector elements employed, as shown in Fig. 5(d). We also observed higher sensitivity for MSOT128 compared to MSOT64 and the highest sensitivity for MSOT256. Similar observations can be made for transversal resolution in 10 mm distance from the array center (microsphere 3): MSOT256 resolves a width of $200 \mu\text{m}$, MSOT128 $300 \mu\text{m}$, and MSOT64 $450 \mu\text{m}$. In relative terms, i.e., from MSOT64 over MSOT128 to MSOT256, improvements in transversal resolution were expected; compared to simulation, however, absolute resolutions seem too high. The explanation for this apparent outperformance of simulation results lies in the necessary light fluence correction and segmentation, which both are non-linear operations but consistent for all arrays. Considering the pixel size of $67 \mu\text{m}/\text{pixel}$, the transversal resolution discrepancy for MSOT256 is ~ 1 pixel, for MSOT128 close to 2 pixels, and for MSOT64 close to 4 pixels. Thus, experimental results from the phantom confirm the superior image quality of MSOT256.

3.3 Mouse Imaging In Vivo

Figure 6 shows the results obtained from the same nude mouse imaged sequentially and without averaging in all three systems. To qualitatively compare achievable imaging performance, we have selected three content-rich anatomical regions of increasing diameter. As the mouse was identically positioned during all three scans and we took 50 frames per position, we were able to

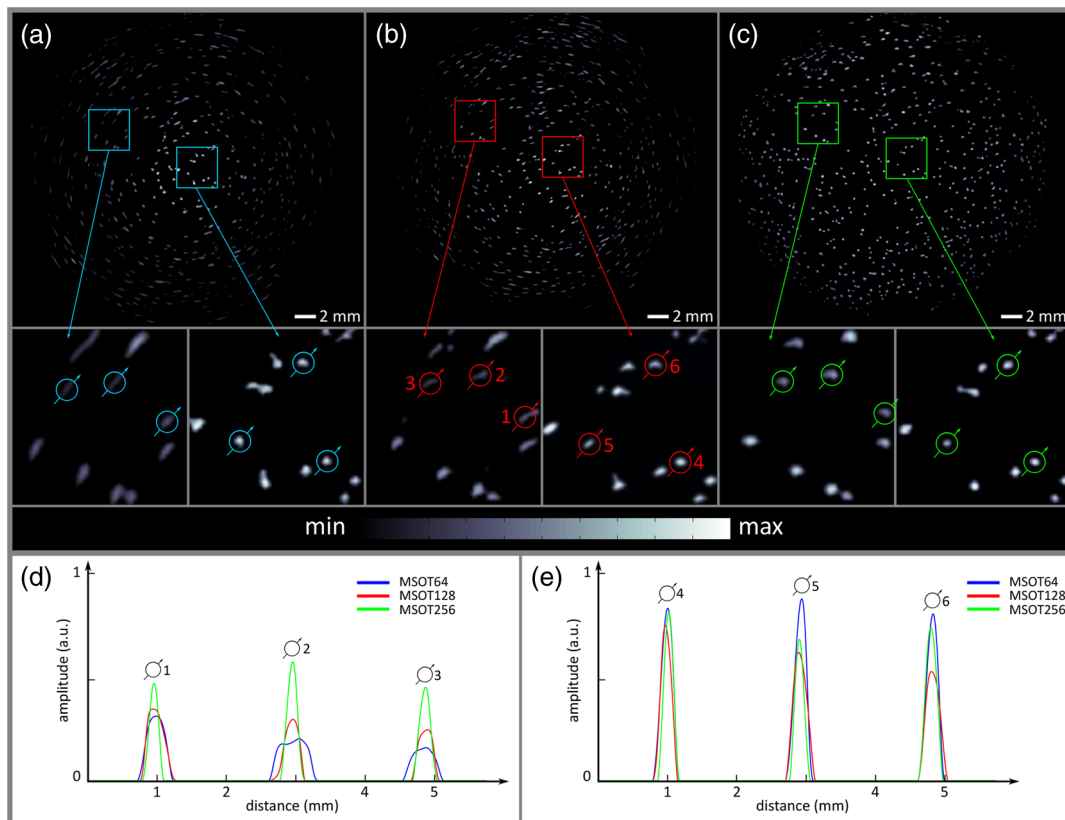


Fig. 5 Top row shows experimental phantom reconstruction results from (a) MSOT64, (b) MSOT128, and (c) MSOT256. For each image, negative values were set to zero and the remainder normalized to 1. Furthermore, images were segmented based on their local maxima. Details at the periphery and the center, framed ($4 \times 4 \text{ mm}^2$) and color-coded by array, were magnified for display at the bottom left and right, respectively. Graphs below depict diagonal cross-sections of individual microspheres (circled blue, red, and green) for (d) the periphery (numbered 1 to 3) and (e) the center (numbered 4 to 6). Individual cross-sections were artificially spaced to allow sufficient distance for comparison.

precisely choose the same cross-sectional image at the same respiratory time point for all three systems. Columns of Fig. 6 show results by system, with the last column depicting cryoslices at equivalent positions from a comparable mouse.

Analysis of the mouse head revealed that all arrays captured large vascular structures on the periphery as well as deep inside the brain. Compared to other body segments, the mouse head was covered reasonably well by all geometries. The temporal artery (marked 2), the sagittal sinus (marked 1), and deep-seated extra-cranial (marked 3) and cerebral blood vessels (marked 4) were visible in all cases. However, closer inspection of Figs. 6(a) to 6(d) reveals improving resolution for increasing number of detector elements. For example, the sagittal sinus is only vaguely captured by MSOT64 with a transversal diameter of $600\ \mu\text{m}$ at its widest point, whereas it is more accurately reconstructed with MSOT128 ($550\ \mu\text{m}$ diameter) and MSOT256 ($450\ \mu\text{m}$ diameter). Similar inspection of the temporal artery revealed a reconstructed size of 670 , 470 , and $380\ \mu\text{m}$ from MSOT64, MSOT128, and MSOT256, respectively. Comparison of the MSOT256 image and the cryoslice photograph on Fig. 6(d) shows that MSOT256 achieves the most accurate reconstruction of vessels over MSOT64 and MSOT128, offering an overall appearance that is very close to the one seen on the photograph.

MSOT results from the liver level are depicted in Figs. 6(e) to 6(h). MSOT64, shown in Fig. 6(e), allows localization of larger features, such as the spinal cord (marked 5), the aorta (marked 6), or the vena cava (marked 7). However, several anatomical

details in the periphery of the animal are lost, consistent with the findings in Figs. 4 and 5. Conversely, MSOT128, Fig. 6(f), and MSOT256, Fig. 6(g), reveal finer structures and more elaborate views of vasculature showing improved peripheral resolution and fewer artifacts.

Similar observations were obtained from images at the kidney region, where the diameter of the mouse body was $\sim 23\ \text{mm}$. Figure 6(i), obtained from MSOT64, exhibits resolution drop and visualization of coarse features, especially in the animal periphery as in Fig. 6(e) and affords only limited transversal resolution. Nonetheless, characteristic landmarks (spinal cord, aorta, vena cava) and large organs (both kidneys marked 11, spleen marked 12) can be identified. Figure 6(j) depicts the MSOT128 result and shows better clarity in resolving anatomical features compared to MSOT64. As expected from the liver cross-section, the best image quality is achieved by MSOT256, depicted in Fig. 6(k). The significantly improved transversal resolution and sensitivity field is best demonstrated in the right kidney (marked 11).

Due to its feature-rich content, the liver region enables a detailed comparison of cryosection and MSOT images. Figure 7 compares the performance of MSOT256 against a corresponding cryoslice photograph serving as the gold standard, to offer a more elaborate explanation of the signals observed on the optoacoustic images. Five significant landmarks have been encircled and numbered (1 to 5), whereby higher brightness in the MSOT image, Fig. 7(a), corresponds to darker colors in the

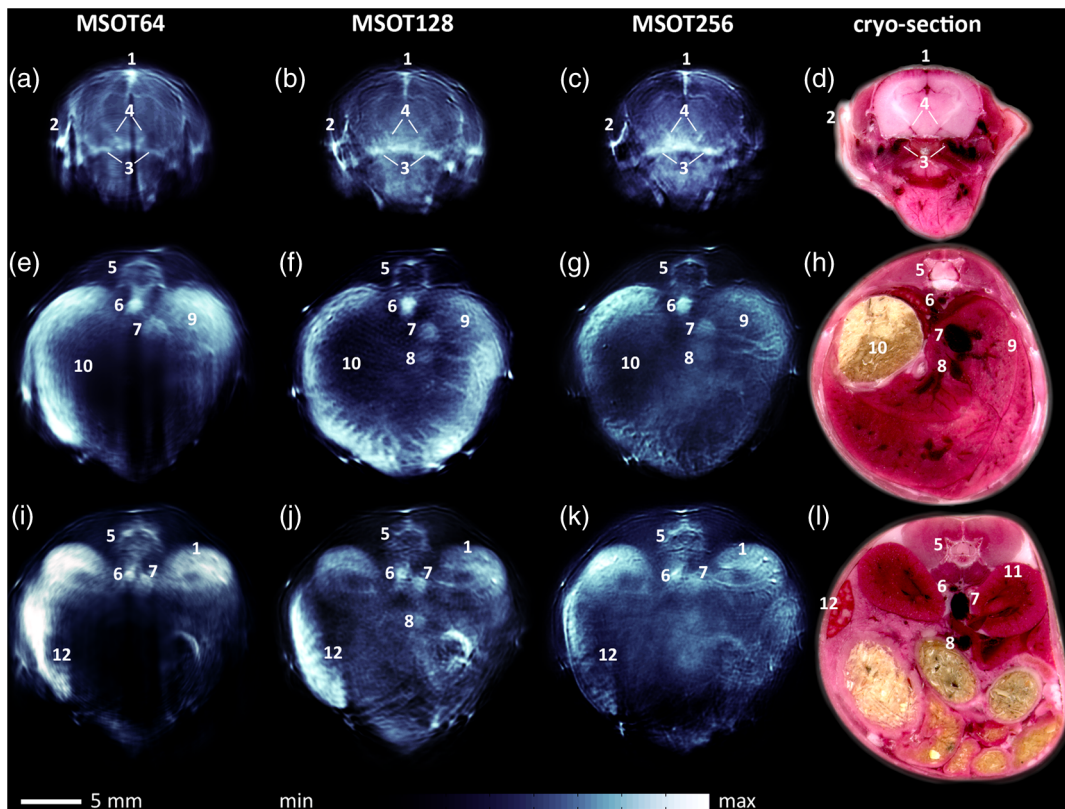


Fig. 6 Single-shot *in vivo* mouse images at 850 nm wavelength: the first column shows results obtained from MSOT64, second column that from MSOT128, and third column that from MSOT256. The last column shows mouse cryoslices at equivalent positions. The mouse head is shown in (a) to (d): 1. sagittal sinus; 2. temporal artery; 3. extra-cranial blood vessel; 4. deep cerebral vessel. The liver region is shown in (e) to (h): 5. spinal cord; 6. aorta; 7. vena cava; 8. vena porta; 9. liver; 10. stomach. The kidney region is shown in (i) to (l): 11. kidney; 12. spleen.

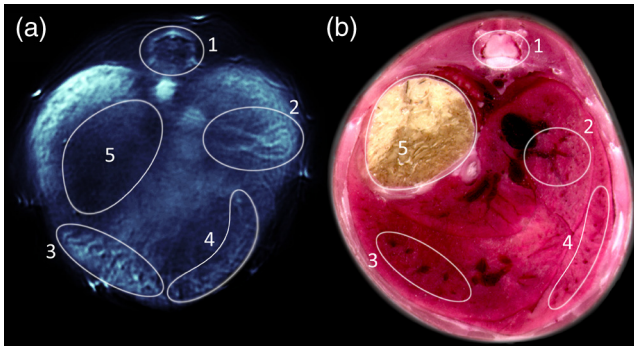


Fig. 7 Mouse cross-section at the liver level. (a) MSOT256 result *in vivo* at 900 nm wavelength. (b) Equivalent cryoslice obtained from a similar mouse. Corresponding features have been encircled and numbered: 1. Spinal cord; 2 to 4. vascular structures within the liver; 5. stomach.

cryosection, Fig. 7(b). The first landmark marks the vasculature surrounding the spinal disk; its structure comprises a bright dot at the center top, which is characteristic of a blood vessel perpendicular to the imaging plane, and a surrounding bracket indicating blood vessels in-plane. Landmarks 2 to 4 highlight different regions within the liver. Area 2 is dominated by elongated in-plane vasculature bifurcating from the vena cava and vena porta toward the periphery. On the other hand, areas 3 and 4 contain vessels perpendicular to the imaging plane—bright dots that correspond to dark dots in the cryosection. Additionally, MSOT highlights short branches originating from these dots. Such features can be attributed to vascular

branching close and perpendicular to the imaging plane. Finally, we also marked the stomach (area 5) because of its prominent position and sharp boundary.

To better understand the relative *in vivo* performance of the three systems employed, Fig. 8 offers a quantitative comparison between the reconstructions obtained by the 64-, 128-, and 256-element systems on the spinal disk. Image profiles taken from the radial and transversal directions (marked r and t) are highlighted in Fig. 8(a) as dashed (MSOT64), dotted (MSOT128), and solid (MSOT256); corresponding traces are shown in Figs. 8(b) and 8(c). A blood vessel perpendicular to the imaging plane was selected to mark the intersection point for orientation purposes. This vessel could be resolved with 128 and 256 elements, but not with 64 due to its close proximity to the top and sides of the surrounding structure. The radial profile illustrates how the transversal resolution of the three systems can affect the result. In MSOT64, the vessel and the adjacent top edge are fused with emphasis given to the edge. In MSOT128, the vessel gives the strongest signal, however, it cannot be resolved from the edge. Finally, only MSOT256 is able to clearly determine the distance between the two as 280 μm (peak to peak). On the other hand, from the transversal profile, the vessel diameter can be resolved as 560 μm using MSOT128 and as 350 μm with MSOT256. MSOT64 again cannot resolve the vessel due to a lack of sensitivity and transversal resolution.

4 Discussion

We studied the MSOT performance achieved in whole-body small animal imaging as a function of increasing number of detectors. Performance was studied numerically and experimentally on

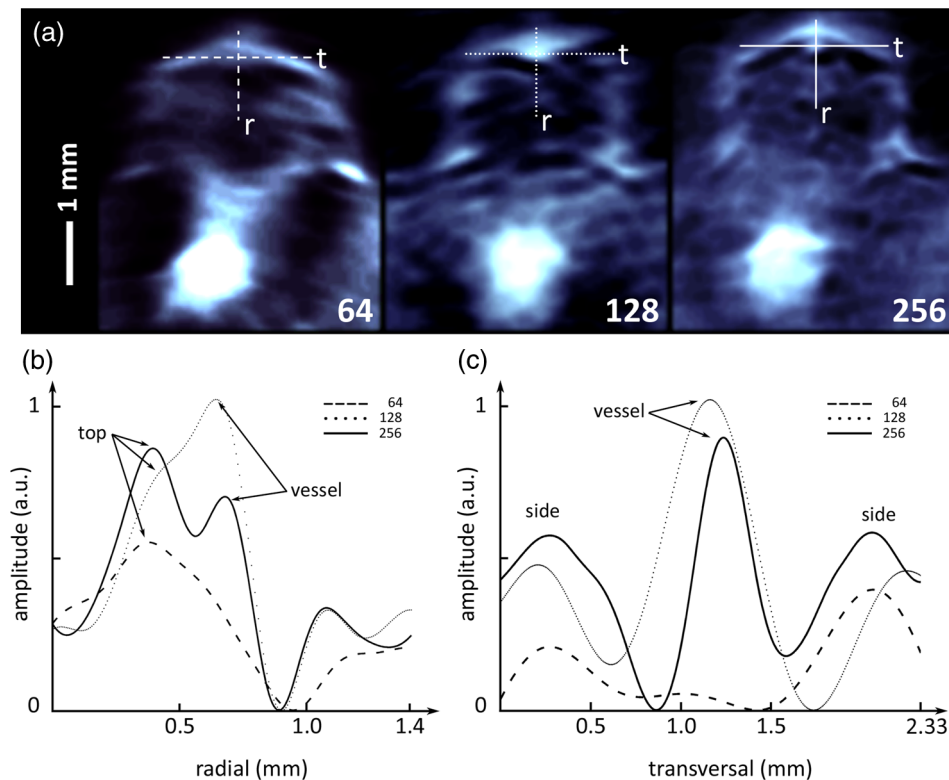


Fig. 8 Profiles of spinal cord at liver level. (a) Magnifications for MSOT64, MSOT128, and MSOT256. Cuts in radial (marked r) and transversal (marked t) directions are line-coded by array. (b) Profile of radial trace from top to bottom. (c) Profile of transversal trace from left to right. Prominent features: top and sides of in-plane vascular structure, blood vessel perpendicular to the imaging plane.

phantoms and animals *in vivo*. The results highlighted improvements in resolution, ROI, sensitivity, and imaging artifacts with increasing angular coverage and detector density. An important finding was that the use of 256 elements yielded strong improvements over 128 elements, to justify deployment of high-density arrays. Qualitatively, the *in vivo* mouse images obtained using 256 elements showcased better resolution and image fidelity over those obtained using 64 or 128 elements, allowing the visualization of elaborate vascular patterns in the brain, spine, kidney, or liver. In a controlled phantom measurement, we experimentally quantified the improvements. At the critical radius of 10 mm from the image center, transversal resolution increased by a factor of 2.25 for 256 elements and 1.5 for 128 elements when compared to results from the 64-element system. Similarly, sensitivity at this radius improved for 128 elements by ~50% and ~150% for 256.

Besides higher resolution, an interesting feature identified in this study is that the FOV can be improved without sacrificing sensitivity when employing more transducers. Given the same azimuthal coverage, the 256-element array achieves a sensitivity field that is broader than the 128, which enables the use of larger animals. In Ref. 14, an array of even higher density was utilized and demonstrated cross-sectional full-body imaging using ring illumination after 10 times averaging, whereby an image represented a time interval of 16 s. In contrast, images presented herein were obtained from a single laser pulse, i.e., 50 μ s acquisition time per image. This enables an achievable frame rate that depends on the repetition rate of the laser only (10 Hz in our setups). Similarly, results from MSOT256 show that to obtain high-quality images, full view is not mandatory but can be reduced when choosing appropriate system radius and element size. However, in the presence of strong acoustic heterogeneities, such as the lungs or gas-filled gastrointestinal tract, the missing angular coverage results in stronger artifacts than would be the case at full view. In sum, the most important parameter in terms of resolution and FOV is element pitch—the smaller the better. Beyond that, array density improves the signal-to-noise ratio as it acts as a form of averaging. Second, the array should cover sufficient views to include the ROI in the visibility region, as defined in Fig. 2. Nonetheless, more views improve available information and enable a more stable reconstruction, especially in the presence of strong acoustic heterogeneities. Finally, the displacement of elevation focus of individual elements ($R_{se} = 37$ mm) versus in-plane focus of the array ($R_A = 40$ mm) increases the sensitivity field.

An additional inference, however, from these observations relates to quantification. As Fig. 2 shows, sensitivity drops significantly with increasing radius from the array center. Combined with possible inhomogeneity in illumination patterns, this can lead to quantification differences for objects placed at different areas in the imaging plane. Using the study performed herein, such inhomogeneity can be well characterized, in particular detector sensitivity, which is an implicit characteristic of element and array geometry. The sensitivity field of each transducer, therefore, needs characterization and implementation in the inversion code to achieve correct quantification across the imaging plane.

For many biological applications, the use of MSOT64 can be regarded sufficient as it still provides a marked improvement over 2-D optical imaging systems or tomographic implementations, which attain 10 times worse resolution. However, with the documented higher transversal resolution and image

quality established by the MSOT128 or the MSOT256, these systems offer superior performance and should be preferred for achieving an all-around better imaging quality. With the MSOT256 yielding the larger FOV (FWHM sensitivity field) and resolution of the three systems studied, scanning of larger animals or the use of more challenging animal models becomes interesting.

Nonetheless, challenges remain. While a 2-D image is derived from a consistent, motion-free dataset, the full-body scan, i.e., the 3-D dataset, cannot be acquired in real time. Improvements in laser repetition rates and continuous translation implements could lead to fast 3-D scans with the geometrical implementations considered herein. Since it is unlikely that truly real-time 3-D systems can be widely disseminated, as they would come at a very high cost, 2-D curved array systems will possibly remain a reasonable option not only for 2-D imaging but also for 3-D scans.

References

1. J. S. Lewis et al., "Small animal imaging: current technology and perspectives for oncological imaging," *Eur. J. Cancer* **38**(16), 2173–2188 (2002).
2. R. A. de Kemp et al., "Small-animal molecular imaging methods," *J. Nucl. Med.* **51**(Suppl. 1), 18S–32S (2010).
3. V. Ntziachristos, "Going deeper than microscopy: the optical imaging frontier in biology," *Nat. Methods* **7**(8), 603–614 (2010).
4. A. Rosencwaig and P. R. Griffiths, "Photoacoustics and photoacoustic spectroscopy," *Phys. Today* **34**(6), 64–66 (1981).
5. R. A. Kruger, "Photoacoustic ultrasound (PAUS)—reconstruction tomography," *Med. Phys.* **22**(10), 1605–1609 (1995).
6. A. Taruttis et al., "Multispectral optoacoustic tomography of myocardial infarction," *Photoacoustics* **1**(1), 3–8 (2013).
7. D. Razansky, C. Vinegoni, and V. Ntziachristos, "Multispectral photoacoustic imaging of fluorochromes in small animals," *Opt. Lett.* **32**(19), 2891–2893 (2007).
8. X. Wang et al., "Noninvasive laser-induced photoacoustic tomography for structural and functional *in vivo* imaging of the brain," *Nat. Biotechnol.* **21**(7), 803–806 (2003).
9. R. Ma et al., "Multispectral optoacoustic tomography (MSOT) scanner for whole-body small animal imaging," *Opt. Express* **17**(24), 21414–21426 (2009).
10. E. Z. Zhang et al., "In vivo high-resolution 3D photoacoustic imaging of superficial vascular anatomy," *Phys. Med. Biol.* **54**(4), 1035 (2009).
11. V. Kozhushko et al., "Focused array transducer for two-dimensional optoacoustic tomography," *J. Acoust. Soc. Am.* **116**(3), 1498–1506 (2004).
12. H.-P. Brecht et al., "Whole-body three-dimensional optoacoustic tomography system for small animals," *J. Biomed. Opt.* **14**(6), 064007 (2009).
13. L. Song et al., "Fast 3-D dark-field reflection-mode photoacoustic microscopy *in vivo* with a 30-MHz ultrasound linear array," *J. Biomed. Opt.* **13**(5), 054028 (2008).
14. J. Xia et al., "Whole-body ring-shaped confocal photoacoustic computed tomography of small animals *in vivo*," *J. Biomed. Opt.* **17**(5), 050506 (2012).
15. R. A. Kruger et al., "Photoacoustic angiography of the breast," *Med. Phys.* **37**(11), 6096–6100 (2010).
16. A. Bühler et al., "Three-dimensional optoacoustic tomography at video rate," *Opt. Express* **20**(20), 22712–22719 (2012).
17. L. Xiang et al., "4-D photoacoustic tomography," *Sci. Rep.* **3**, 1113 (2013).
18. A. Buehler et al., "Video rate optoacoustic tomography of mouse kidney perfusion," *Opt. Lett.* **35**(14), 2475–2477 (2010).
19. A. Buehler et al., "Real-time handheld multispectral optoacoustic imaging," *Opt. Lett.* **38**(9), 1404–1406 (2013).
20. A. Taruttis et al., "Fast multispectral optoacoustic tomography (MSOT) for dynamic imaging of pharmacokinetics and biodistribution in multiple organs," *Plos One* **7**(1), e30491 (2012).

21. N. C. Burton et al., "Multispectral opto-acoustic tomography (MSOT) of the brain and glioblastoma characterization," *Neuroimage* **15**(65), 522–528 (2012).
22. E. Herzog et al., "Optical imaging of cancer heterogeneity with multispectral optoacoustic tomography," *Radiology* **263**(2), 461–468 (2012).
23. A. Dima and V. Ntziachristos, "Non-invasive carotid imaging using optoacoustic tomography," *Opt. Express* **20**(22), 25044–25057 (2012).
24. J. A. Jensen, "Field: a program for simulating ultrasound systems," *Med. Biol. Eng. Comput.* **34**(Suppl. 1, Part 1), 351–353 (1996).
25. J.A. Jensen and N. B. Svendsen, "Calculation of pressure fields from arbitrarily shaped, apodized and excited ultrasound transducers," *IEEE Trans. Ultrason., Ferroelectr., Freq. Control* **39**(2), 262–267 (1992).
26. Y. Xu et al., "Reconstructions in limited-view thermoacoustic tomography," *Med. Phys.* **31**(4), 724–733 (2004).
27. A. Buehler et al., "Model-based optoacoustic inversions with incomplete projection data," *Med. Phys.* **38**(3), 1694–1704 (2011).
28. D. Razansky, A. Buehler, and V. Ntziachristos, "Volumetric real-time multispectral optoacoustic tomography of biomarkers," *Nat. Protocols* **6**(8), 1121–1129 (2011).
29. A. Rosenthal, D. Razansky, and V. Ntziachristos, "Fast semi-analytical model-based acoustic inversion for quantitative optoacoustic tomography," *IEEE Trans. Med. Imaging* **29**(6), 1275–1285 (2010).
30. G. J. Diebold and P. J. Westervelt, "The photoacoustic effect generated by a spherical droplet in a fluid," *J. Acoust. Soc. Am.* **84**(6), 2245–2251 (1988).

Alexander Dima received a Dipl.-Ing in electrical engineering and information technology in 2009 from the Technical University of Munich. He is currently pursuing his PhD at the Chair for Biological Imaging under guidance of professor Vasilis Ntziachristos. His research focuses on the application of optoacoustic imaging to non-invasive clinical diagnosis and intraoperative imaging.

Neal C. Burton is currently a senior application specialist at iThera Medical. His main activities at iThera Medical include oversight of application development of optoacoustic clinical imaging as well as the publication of preclinical optoacoustic imaging studies in pharmacology and cancer models in small animals. His research interests, expertise, and publications include models of neurodegeneration, toxicology, cancer, antioxidant protection against chronic disease, optical and optoacoustic imaging, and public health.

Vasilis Ntziachristos studied electrical engineering at Aristotle University in Thessaloniki, Greece, and received his MSc and PhD from the Bioengineering Department of the University of Pennsylvania. He served as an assistant professor and director of the Laboratory for Bio-Optics and Molecular Imaging at Harvard University and Massachusetts General Hospital. His research encompasses the development of new methods and devices for biological and medical imaging focusing on innovative noninvasive approaches that visualize previously unseen physiological and molecular processes in tissues.